HiSST: 3rd International Conference on
High-Speed Vehicle Science Technology
14 -19 April 2024, Busan, Korea

Investigation of Detonation Wave Phenomena in Non-Premixed H_2-Air Annular Rotating Detonation Combustor using Large-Eddy Simulation

Y. Lim[*1], T. Nilsson*[*2] & C. Fureby*[*3]*

Abstract

A series of Large Eddy Simulation (LES) based investigations was performed to analyse a non-premixed hydrogen-air annular rotating detonation combustor, using a detailed 22-step reaction mechanism and a finite volume based solver previously-designed for high-speed reacting flows. A specific design and test configuration from the US Air Force Research Laboratory has been used. The mass flow rate was maintained at 0.144 kg/s, with a unity global equivalence ratio for the reactant inflows, throughout the simulations. The results obtained from the single stably-rotating wave, showcase the computational model's capability to replicate the principal characteristics of rotating detonation waves. Validation of the numerical results with available experimental data, shows agreement in magnitude and trend. Statistical analysis revealed increased temperature and pressure, volumetric expansion, and fuel suppression during and after the wave sweep, resulting in higher outer wall temperatures in the front axial half of the combustor. The role of reactant mixing in the studied rotating detonation case was also evaluated. Wide ranges of temperature and pressure were observed within the combustor, highlighting the highly dynamic nature of the combustion processes. A significant amount of deflagration was also found to be present in the chamber, with those occurring ahead of the detonation wave having a potentially more significant impact on the combustor performance.

Keywords: *rotating detonation, non-premixed, large-eddy simulations, hydrogen-air.*

Nomenclature

Latin
p_{ch} – instantaneous static pressure
$\langle p_{ch} \rangle$ – time-averaged static pressure
$\dot{Q}$ – heat release rate
T_{ch} – instantaneous static temperature
$\langle T_{ch} \rangle$ – time-averaged static temperature
Y – mass fraction
Z – mixture fraction

Subscripts
ch – chamber
st – stoichiometric

1. Introduction and Background

Utilising pressure-gain combustion, the Rotating Detonation Engine (RDE) is one of the more recent and promising candidates that might offer a breakthrough in aircraft propulsion technology. Based on a rotating detonation wave(s) in an annular combustion chamber that both compresses and ignites the reactants, resulting in chemical heat release and volumetric expansion, RDEs could potentially give rise to novel and compact engine designs. Theoretically, this detonation-based combustion process offers higher flow and heat release rates [1] and lower entropy rise [2], resulting in higher thermodynamic efficiency [3]. This could contribute towards a more powerful or compact engine, one that could even propel high-speed flight. The simplicity of needing only a single ignition to start off continuous operation also puts RDEs ahead of other competing detonative combustion engines.

[*]*Lund University, Department of Energy Sciences; Lund, PO Box 118, SE 221-00, Sweden*
[1]*yuxiang.lim@energy.lth.se;* [2]*thommie.nilsson@energy.lth.se;* [3]*christer.fureby@energy.lth.se*

Although there has been a large and still rapidly growing number of theoretical, experimental, and numerical RDE studies, the underlying unsteady and multi-scale physical process remains inadequately comprehended. Premixed RDEs offer the benefit of well-mixed reactants which in turn give a greater probability of achieving stable detonations [4], but also bring several operational challenges, such as the hazard of flashback, difficulties to control [5], and very restricted operational durations because of high temperatures. These challenges have contributed to the pivoting of experimental work towards non-premixed RDE configurations in recent times [6-8].

On the other hand, injecting fuel and oxidiser individually into the combustion chamber makes mixing one of the performance-limiting factors [2], which can result in wave speed reductions in the range of 30% [9]. To counter this problem, numerous improved designs involve injecting reactants into the combustion chamber as impinging jets [7, 8, 10-12]. It could be inferred that non-premixed RDEs add another level of complexity – unsteady reactant mixing – on top of existing ones such as numerous conflicting detonation waves, large heat losses, detonation boundary layer interactions, chaotic start-up and parasitic combustion, which are all awaiting understanding and solution.

From another perspective, the extraordinary rapidly-evolving flow dynamics in rotating detonation, intertwined intricately with areas of fluid compressibility, flow discontinuity, combustion chemistry, and different heat transfer modes, presents a high barrier to theoretically-conclusive experimental research. The considerable expenses and sophistication of RDE experiments have spurred recent efforts in computational research in this field. Simulations not only facilitate fast and effective parametric studies to assist in the design work, but could also offer an exclusive platform to visualise occurrences within the flow fields and probe the fundamental mechanisms behind them. Combining results from both experimental investigations and numerical simulations can provide the unparalleled avenue to investigate some of the key physical principles behind the detonation wave phenomena, which might not be practically achievable with experiments alone.

Even with the integration of experimental and simulation techniques, there still exists a wide knowledge gap in terms of comprehension of rotating detonation principles. The interdependent processes of mixing and burning within time-scales of O(μs), as well as intense flow intricacy and conditions, demand resolving finely in both time and space. With the resultant sky-high requirements of computational resources for investigating rotating detonations, it is unsurprising that many numerical studies fall back on practical simplifications, such as two-dimensional analyses [13-15], applying Reynolds Averaged Navier-Stokes (RANS) models [16, 17], using premixed reactants [15, 16, 18-22], and running with simpler (single step) chemical reaction mechanisms [4, 13, 16, 20, 21, 23].

In this study, Large Eddy Simulations (LES) have been coupled with finite-rate chemistry to run high-fidelity calculations of flows within a non-premixed Rotating Detonation Combustor (RDC). The main aim of this paper is to document the findings from the evaluation of reactant mixing and rotating detonation wave characteristics. The model RDC of choice, designed by the US Air Force Research Laboratory (AFRL) [24], utilises jets-in-crossflow injection to promote reactant mixing. The design has been comprehensively investigated via both experimental [24-27] and numerical [28, 29] methodologies, offering a rich database of data on top of a pragmatic design and accessible information. The simulations are performed with a previously-developed solver designed for high-speed flows, in the OpenFOAM 7.0 environment, in a bid to provide insights into the complex dynamics in the RDC. Instantaneous and time-averaged results are analysed to illustrate macroscopic effects that the combustion processes have on flow fields. The statistical tool of conditional averaging is applied to flow parameters and species, to explore links between the detonation wave structure and mixing.

2. Computational Modelling

This section introduces the numerical techniques employed in this investigation. More specifically, Section 2.1 discusses the choice and specifics of LES, particularly the use of implicit LES with built-in subgrid modelling, and its underlying principles. The numerical methods utilised for solving the governing equations, are also covered. Section 2.2 compares various chemical reaction mechanisms for hydrogen (H_2)-air combustion, against experimental data, to justify the one adopted in this research.

2.1 Large Eddy Simulation Modelling

The fundamental concept of Computational Fluid Dynamics (CFD) revolves around the solution of equations involving mass, momentum, energy, and species mass fractions originating from Newton's

equations of motion and the first law of thermodynamics. The variables of density, ϱ, pressure, p, temperature, T, and composition, Y_i, are linked up by thermodynamic equations of state. On the other hand, constitutive equations are used to characterise the fluid mixture, which is treated as possessing a Newtonian fluid behaviour, along with Fourier heat conduction and Fick's law of mass diffusion. The modelling of species viscosities, diffusivities, thermal conductivities [30] in this case are based on Sutherland's Law, constant Schmidt numbers for each species, and Prandtl number. With the law of mass action, the Arrhenius reaction rates are summed up to obtain the species reaction rates [31]. Additionally, the combustion chemistry in reacting flows is accounted for via a network of chemical reactions.

For many CFD applications, there exist three types of turbulence modelling: Direct Numerical Simulation (DNS), LES, and RANS, listed here in the order of increasing modelling. DNS lies at one extreme of the range, resolving all scales of turbulence directly in the absence of any form of modelling. At the opposite end of the spectrum, RANS relies on turbulence models to account for the fluctuations, while only solving for the mean flow. Although DNS offers exclusive precision and flow details, it demands astronomical amounts of computational resources. The third option of LES stands in the middle, striking a balance between computational efficiency and accuracy. LES thus has its attractive advantages for the simulation of non-premixed RDC's, where unsteady phenomena like reactant mixing, post-ignition transitions, and wave mode shifts are critical. This is especially relevant as RANS is inadequate for capturing the transient dynamics in non-premixed RDC's [32], justifying the choice of LES in this research [4].

Implicit LES (ILES), in which subgrid stress and flux terms are modelled with the leading-order truncation error of the numerical scheme [33-35], is employed in this investigation. A Modified Equation Analysis (MEA) is utilised for the derivation of the implicit subgrid stress and flux terms [36]. A stable and efficient ILES model can be developed using a carefully selected flux reconstruction scheme for the convective fluxes, which usually involves a flux limiter function. This model seeks to handle the equations of reacting flows through the use of implicit models for subgrid stresses, as well as non-oscillatory Finite Volume (FV) methods [37]. The only difference between the implicit and explicit terms, is the representation of the subgrid viscosity with a fourth-rank tensor in the former case, and thus accounting for simultaneous flow and grid anisotropies. Although ILES models possess the advantageous ability of handling concurrent flows and mesh irregularities [33], their performance is influenced by the choice of flux-limiting schemes, with those that preserve monotonicity being the most robust.

The omission of a turbulence-chemistry interaction model, as employed here to deal with the filtered chemistry source terms, is a potential point for debate. The justification is we have yet to understand how detonation waves and small-scale turbulence interact, and also the performance of available LES combustion models on simulating detonation and RDC phenomena. Therefore, we made this selection, in view of the further research required in this aspect.

The simulations are run with the second-order accurate FV method as implemented in OpenFOAM 7.0 [36]. Despite the popularity of low-dissipation schemes due to their ability to resolve turbulence, they have problems with flow discontinuities common in high-speed flows. The introduction of numerical diffusion and dissipation [38], as well as a variety of flux evaluation schemes [39], could be used to address this limitation. In addition, a density-based, fully explicit, solver is used together with the Kurganov-Tadmor flux reconstruction scheme [40]. The combustion chemistry is solved separately using a Strang splitting approach [41], while the combustion chemistry is integrated in time with a Rosebrock solver [42]. Lastly, a variable time-step keeps the Courant number below 0.5.

2.2 Combustion Chemistry

Findings from prior research have highlighted the significance of selecting an appropriate chemical reaction mechanism for LES of high-velocity deflagration processes [43, 44]. A basic comparison has been conducted across a spectrum of chemical reaction mechanisms, from simple global ones to those with more detailed processes. The one-step M1 [45]; seven-step skeletal mechanisms of ES7 [46], BG7 [47], and D7 [48]; and detailed ones such as J20 [49], K30 [50], USCII [51], and Z22 [52] containing at least twenty reactions, were evaluated. The Z22 was designed specifically for H_2-air ignition and combustion, and consists of 9 species and 22 irreversible reactions with an additional three reactions

for fuel decomposition [53]. Furthermore, the mechanism incorporates the H_2-O_2 structural model from an earlier pathway-centric reaction mechanism [53].

Consistent with the conventional assessment for combustion processes, the performance of the chosen reaction mechanisms was evaluated by looking at laminar speed (s_u), ignition delay time (τ_{ign}), and extinction strain rate (σ_{ext}) at 1 atm pressure. Fig. 1a, Fig. 1b, and Fig. 1c display the trends for s_u, τ_{ign} and σ_{ext}, for each mechanism alongside experimental data.

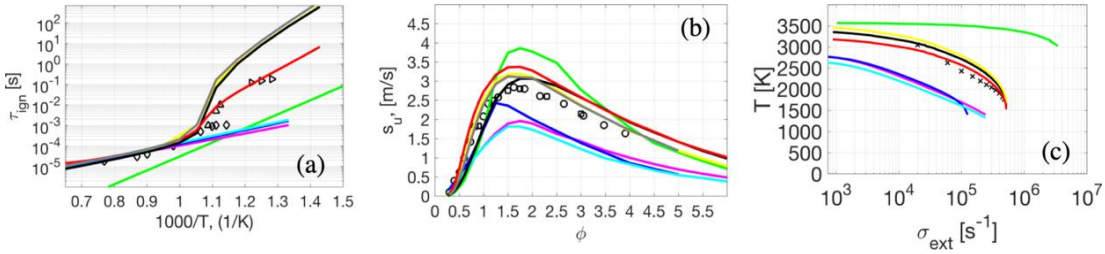

Fig 1. Plots of (a) ignition delay times against 1000/T; (b) laminar flame speeds against equivalence ratios; (c) temperatures against extinction strain rate. Legend: (—) M1 [45], (—) ES7 [46], (—) BG7 [47], (—) D7 [48], (—) J20 [49], (—) K30 [50], (—) USCII [51], (—) Z22 [52], and experimental data (symbols) from [54-59].

Based on the τ_{ign} graph in Fig. 1a, the various mechanisms fare similarly at temperatures higher than ~1000 K. However, significant variations emerge at temperatures below this threshold, particularly in the ~850 K to ~1000 K range. Mechanisms comprising seven or fewer reactions fail to reproduce the distinct kink of the experimental data-points, because of the absence of H_2O_2 and HO_2 chemistry. In contrast, the majority of the detailed mechanisms over-exaggerate the curve within this range, resulting in prolonged τ_{ign} periods for temperatures above ~900 K. On the contrary, the Z22 successfully replicates the experimental trends within the interval, aligning with mechanism's design objectives [52].

In Fig. 1b, the data for s_u shows that Z22, J20, K30, and USCII closely match the experimental points. The mechanisms with less reaction steps show deviations, with M1 overshooting and the seven-step ones falling short of the experimental points. Similarly, the same detailed mechanisms show consistency with the experimental σ_{ext} values in Fig. 1c, whereas the other four simpler mechanisms demonstrate the same signs of respective overestimation and underestimation.

The above-mentioned factors justify the selection of Z22 as the reaction mechanism for the RDE simulations subsequently discussed.

3. Computational Set-Up

The following section presents information on the computational model's configuration used in this investigation. In Section 3.1, the RDC hardware design and the computational adaptations are discussed. The simulations' initial and boundary conditions are outlined in Section 3.2.

3.1 RDC Design and Computational Grid

To advance our understanding of RDC phenomena and concurrently compare the computational model's performance through experimental validation, the well-studied non-premixed RDC design of Rankin *et al* [24] has been selected. The AFRL RDC design was simplified with the key geometrical features retained, resulting in the 3D model that is used in this study. Fig. 2a shows a cross-section of the actual annular RDC design. The simulation model shares the same corresponding dimensions of 53.9 mm, 138.7 mm and 101.6 mm, for the outer and inner diameters, and axial length, respectively.

Rankin *et al* [24] investigated multiple configurations of air and fuel injector dimensions. The configuration chosen for our numerical campaign features an air slot of 3.56 mm, along with 120 H_2 injectors each measuring 0.89 mm in diameter. The height and area of the air inlet are exactly replicated in the computational model as a radial slot on the inner annular wall, whereas the fuel inlets are represented as cuboids with 0.789 mm squares of area equivalent to the circular injectors in the hardware. The air inlet is demarcated in pink, and the chamber walls in blue and green, in Fig. 2b which also shows the 120 squarish fuel injectors. The 3D model mimics identically the hardware's annular thickness of 7.6 mm, which is also visible in the sliced domain in Fig. 2b, throughout the entire axial length.

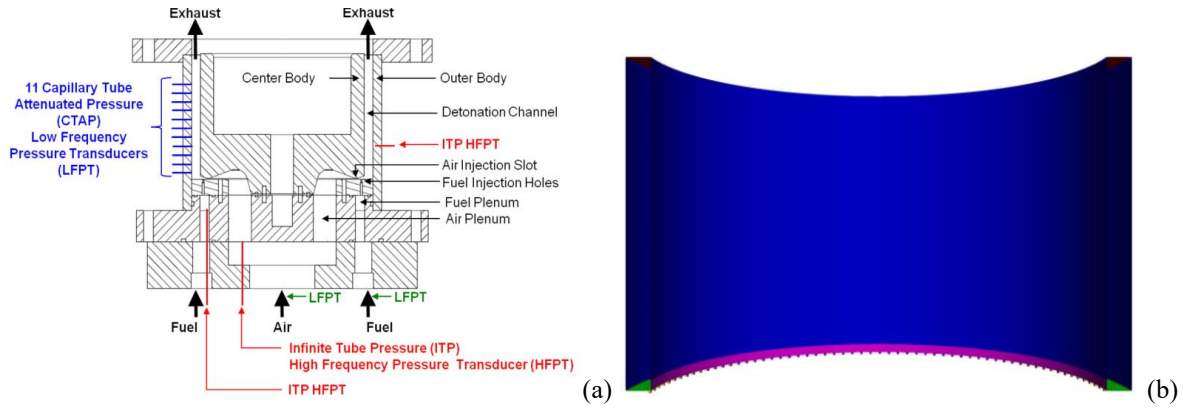

Fig 2. (a) Adopted RDC design's cross-section, showing flow passages and transducer locations [24]. (b) Computational model displaying fuel (small tubes, at bottom of figure) and air (pink) inlets, combustor base (green), inner and outer annular walls (blue), and outlet (top).

Hexahedral, structured and nearly uniform computational grids were used in all simulations in the series. The baseline grid comprises 20.9 million cells, with an individual base size of 0.35 mm.

3.2 Simulation Initialisation and Boundary Conditions

To improve computational cost economy, the simulations were initiated on a coarser grid. Once the detonations achieved a statistically-steady cycle, the data was transferred to the main grid, to continue the run for generation of the key results.

Every simulation began with a pre-flow of reactants for 60 μs. Subsequently, detonation was triggered by inserting a sphere of 20 bars pressure, 1500 K, and a 2000 m/s velocity component tangent to the annulus. This 'ignition zone' spans the full combustor thickness, sparking off tangential detonation waves. The centre of the zone is positioned 15 mm axially away from the point of fuel injection. It is worthy to mention that the numerical 'ignition' method does not seek to exactly replicate that of the actual experiment. Instead, it merely serves as a means to attain the phase of statistically-stable wave rotation, which was also the targeted mode of evaluation in the experiments.

This methodology complements the previously-mentioned strategy of beginning each simulation case with a cost-effective coarse grid, from which the results were not quantitatively examined, before moving to the fine grid for more accurate computation and data analysis. Data analyses are focused on the period in which the detonation waves have reached a statistically-cyclical state.

With respect to boundary conditions, a consistent set is applied across all simulation cases. In summary, inflows are regulated using fixed mass flow rates; a wave-transmissive condition is used at the outlet; fixed temperatures are imposed at inlets; adiabatic walls are applied.

4. Results and Discussion

The following section revolves around the results acquired in the campaign, and the findings arising from the corresponding data processing and evaluation. The first sub-section gives an outline of the simulations with respect to controlled parameters and overall wave behaviour, and Section 4.2 documents the conducted grid independence study. The final two sub-sections detail the results derived from analyses using, respectively, unconditional and conditional statistics.

4.1 Case Study Overview

In this study, the total mass flow rate of reactants is set as 0.1441 kg/s, with a global equivalence ratio of $\phi = 1$. In the simulation campaign, data acquisition was performed after the circling wave had attained a statistically steady mode. A single wave has been predicted in all the LES runs, akin to the wave number witnessed in the corresponding experimental case. The wave frequency of 3.8 kHz has been recorded in the numerical runs, as compared to the 2.7 kHz clocked experimentally.

The instantaneous temperature contour plot of Fig. 3a has been extracted from the main simulation conducted with Mesh II (elaborated in Section 4.2). The capability of the LES model in executing three-

dimensional calculations is highlighted, demonstrating the ability to distinctly identify critical wave formations [60]. Four notable structures are pointed out in the plot: A, the primary detonation wave; B, the associated oblique shock; C, the region with newly-injected reactants; D, the slip line at which hot gases from consecutive cycles meet [61]. The blue regions of cold reactants visible is distinct at front axial end of the annular chamber, just downstream of the fuel injection tubes, prior to a wave sweep.

Similar wave structures are also identified in Fig. 3b, which was experimentally acquired using OH* chemiluminescence. An important note is that the directions of wave propagation in the two images are opposite to each other, arising from initiation in alternate directions.

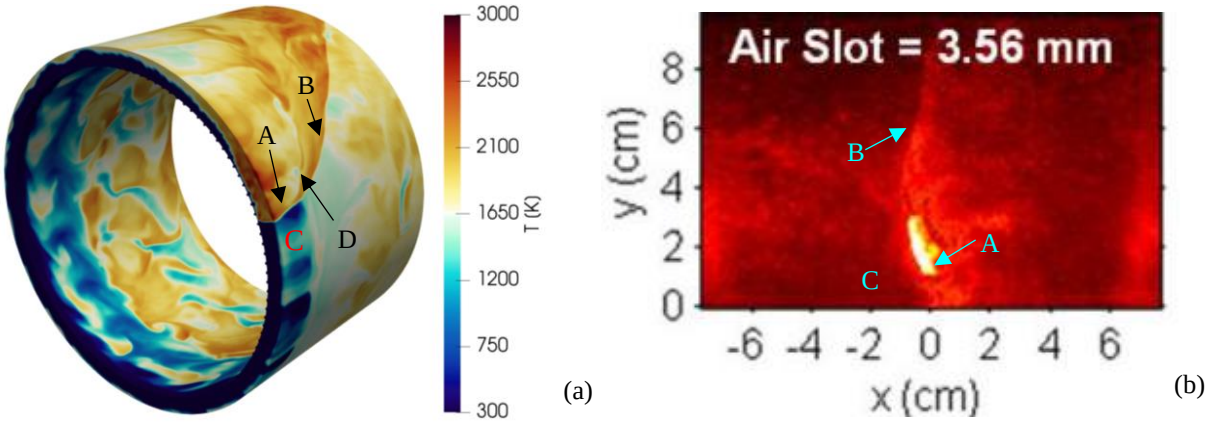

Fig 3. (a) Isometric view showing instantaneous T_{ch} contour plot with the main detonation wave labelled as A, oblique shock as B, reactant refill zone as C, contact slip line as D; and (b) experimental OH* chemiluminescence image [24] showing similar wave structures.

4.2 Grid Sensitivity Study

The impact of grid resolution on the simulation was investigated. This involved three sets of uniformly-structured grids respectively with base sizes of 0.47 mm, 0.35 mm and 0.23 mm. The corresponding cell counts are 6.2 million (Mesh I), 20.9 million (Mesh II) and 49.5 million (Mesh III), respectively. The study contrasted the three datasets, deducing reasonable grid independence between the Meshes II and III. This led to the selection of the 20.9 million-cell grid for the rest of the numerical campaign.

Fig. 4a compares the time-averaged pressure in the axial combustion chamber direction, $\langle p_{ch} \rangle$, across the three grids, supplemented by experimental results [24] for validation. All three curves take after the experimental results fairly well, in terms of both absolute values and variation trend. Except for the upstream portion of the chamber near the injectors, the curve for Mesh I lies clearly below the other two and is also generally flatter and smoother. Among the three datasets, the discrepancy in $\langle p_{ch} \rangle$ between the two finer grids is least pronounced, with significant portions of overlap.

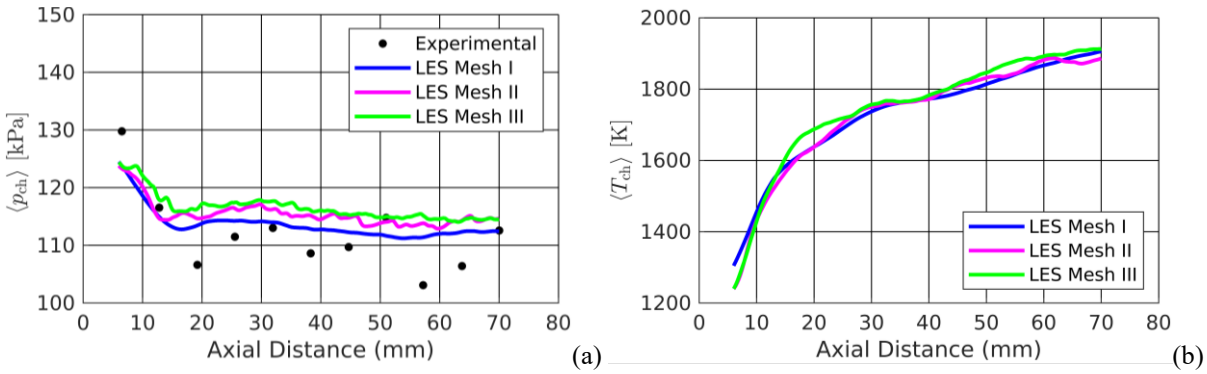

Fig 4. (a) Variations of time-averaged pressure, $\langle p_{ch} \rangle$ with experimental data [24], and (b) temperature, $\langle T_{ch} \rangle$, along axial combustor length for three grids.

Although relevant experimental data is unavailable, the corresponding LES time-averaged temperature, $\langle T_{ch} \rangle$, graph in Fig. 4b points towards the same indication. In fact, the overlapping of the curves take

place to an even larger proportion for this variable. This further signifies acceptable grid insensitivity of Mesh II, which has been adopted for the main study.

A look at the instantaneous temperature, T_{ch}, contour plots on the external annular wall surface also reveals interesting details. Fig. 5a to Fig. 5c present a lateral view of the plots for all three grids, with the wave at roughly the same location. The images provide a visual contrast of the grid resolutions' impact, on the amounts of details that could be extracted from the results. Mesh I is sufficient for resolving only the key parts of the wave, with some rough flow field patterns. In contrast, Mesh II more clearly reveals complex flow dynamics features including the separation of gases between two cycles by a slip line. With the highest resolution, Mesh III is capable of capturing detailed structures, such as vortical patterns that stand out in multiple regions but particularly around the slip line and after the oblique shock, corroborating findings reported in prior studies [60]. The main wave-front shape is noticeably more pronounced in Fig. 5b and Fig. 5c.

Fig 5. Instantaneous temperature, T_{ch}, contour plots of (a) Mesh I, (b) Mesh II and (c) Mesh III, presented in a side-on view.

4.3 Time-Averaged Variation of Flow Fields across Channel Thickness

This sub-section consists of findings from macroscopic and qualitative evaluation of the flow field trends within the combustor. Data generated during the stably-circling wave phase has been time-averaged to illustrate statistical trends of the chamber flow conditions.

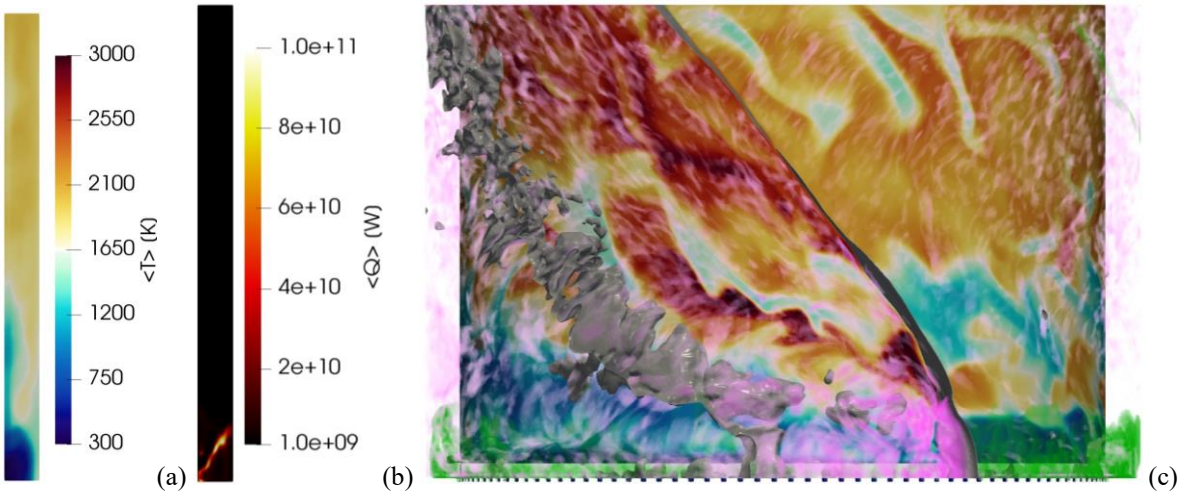

Fig 6. Radial cross-sectional views of time-averaged (a) temperature, $\langle T_{ch} \rangle$, (b) heat release rate, $\langle \dot{Q}_{ch} \rangle$ showing variation of the fields across the channel thickness. (c) superimposed instantaneous temperature, T_{ch}, contour plot in warm colours, constant pressure, p_{ch}, surfaces in grey, volume renderings of H_2 mass fraction in green and expansion, $\nabla \cdot \boldsymbol{v}$, in pink.

Fig. 6a and Fig. 6b are cross-sectional views of time-averaged temperature, $\langle T_{ch} \rangle$, and heat release rate, $\langle \dot{Q}_{ch} \rangle$, respectively. They allow the visualisation of the radial flow field variations across the channel thickness, with the inner wall being on the left and outer wall on the right sides of the images. For the $\langle T_{ch} \rangle$ field, there is a distinct uneven distribution in the lower half of channel near the inlets, with significantly higher temperatures along the outer wall. This phenomenon results from a combination of factors. The first is the inflow of cold reactants from the lower left corner of the image, especially the high-flow air, pushing flow towards outlet and outer wall. The second contribution comes from the

outward expansion of the wave. On the contrary, in the downstream half of the chamber, the temperature is more uniform across the (radial) annular thickness. This is due to the continued consumption of reactants at higher axial heights, in the form of both combustion due to the oblique shock and deflagration when the residual reactants meet the high temperature combustion products, and the hot gases expand and diffuse toward the outlet.

From the $\langle \dot{Q}_{ch} \rangle$ plot of Fig. 6b, it is apparent that the detonation wave originates from the corner of fuel injection as stronger detonations occur at areas of richer mixture as mentioned in literature [62, 63], but expands outwards towards the outer annular wall as noted previously.

Fig. 6c presents an overlay of instantaneous plots for four parameters, extracted from the inner combustor wall. They are namely the T_{ch} contour plot in the background with a blue-orange colour scale, p_{ch} iso-surfaces shown in grey, and volumetric renderings in green representing H_2 mass fraction and pink for $\nabla \cdot \boldsymbol{v}$ which relates to volumetric expansion. A behaviour similar to the previously-mentioned expansive phenomenon could be observed in the azimuthal dimension, where there is a 'forward curving' of the main wave front. The same finding was documented in another study involving RDC high-fidelity simulations [62], and is caused by the annulus curvature's effects on detonation wave expansion. In further analysis of Fig. 6c, the main wave front's passage evidently brings about pressure and temperature spikes, as well as extensive gas expansion, resulting from the rapid reaction and intense energy release resulting from the detonation process. The attached oblique wave also impacts the flow fields through similar trends of volume increase and elevations in T_{ch} and p_{ch}, though by more moderate extents. Another key observation is the sizeable area of volumetric expansion subsequent to the wave's passage which suggests a prolonged time-scale for the spatial effect, relative to the durations of wave propagation and the sustained combustion after the wave. Finally, the discontinuity in the green rendering highlights the momentary suppression of fuel injection caused by heightened pressure levels in and just behind the main wave.

4.4 Statistical Analyses on Detonation Characteristics

In this sub-section, conditional statistics is applied as a quantitative analysis of the simulation results. Conditional averages could offer insights into mechanisms behind systems operating on non-premixed combustion, and also the detailed structure of the burning processes [64].

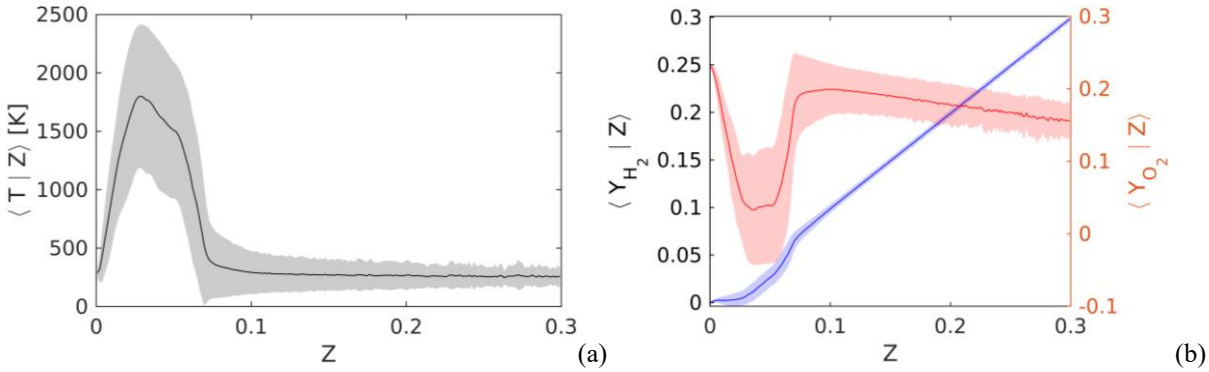

Fig 7. Graphs of mixture fraction-conditioned time-averaged (a) temperature, $\langle T|Z \rangle$, (b) H_2 mass fraction, $\langle Y_{H_2}|Z \rangle$, and O_2 mass fraction, $\langle Y_{O_2}|Z \rangle$.

The graphs in Fig. 7 are derived from the averaging of three variables, based on mass-weighting, and conditioned on mixture fraction, Z. Fig. 7a shows the conditional average temperature, $\langle T|Z \rangle$, with the variance indicated by the shaded area. The peak temperature occurs around the stoichiometric mixture fraction, Z_{st}, of 0.0284. The wide variance, particularly around the highest temperatures, indicate a high degree of spread in temperature in this region of Z values. Possible explanations include the dynamic and potentially unstable nature of the detonation process whose flame structure is possibly dependent on the mixture state, as well as high heat release from strong deflagrations. Additionally, the LES peak temperature falls short of the ideal detonation temperature 2980 K derived from theoretical calculations, substantiating the presence of significant parasitic combustion.

On the other hand, the plot of conditioned H_2 and O_2 mass fractions are shown in Fig. 7b, respectively in blue and red, with their variances. It could be noted $\langle Y_{O_2}|Z \rangle$ has a wide deviation range, also particu-

larly around Z_{st}. Given that the high temperatures in this region is above that for predominant H_2-air chain-branching, it is deduced that the oxidiser fluctuation is a factor that drives the wide temperature variations. The more unstable O_2 could be a sign that the air injection is more affected by the passing detonation wave, through inflow suppression. While the fuel curve is largely in line with conventional concepts for diffusion-based combustion, the conditioned O_2 one indicates presence of significant concentrations of oxidiser after Z_{st}. This suggests the inability of the detonation to consume all the reactants, and the remainder would 'leak' past. The availability of residual O_2 at rich Z potential leads to the slightly asymmetrical shape of the $\langle T|Z \rangle$ curve around the stoichiometric peak, with temperatures not falling as fast on the rich side as mixture fraction departs from Z_{st}.

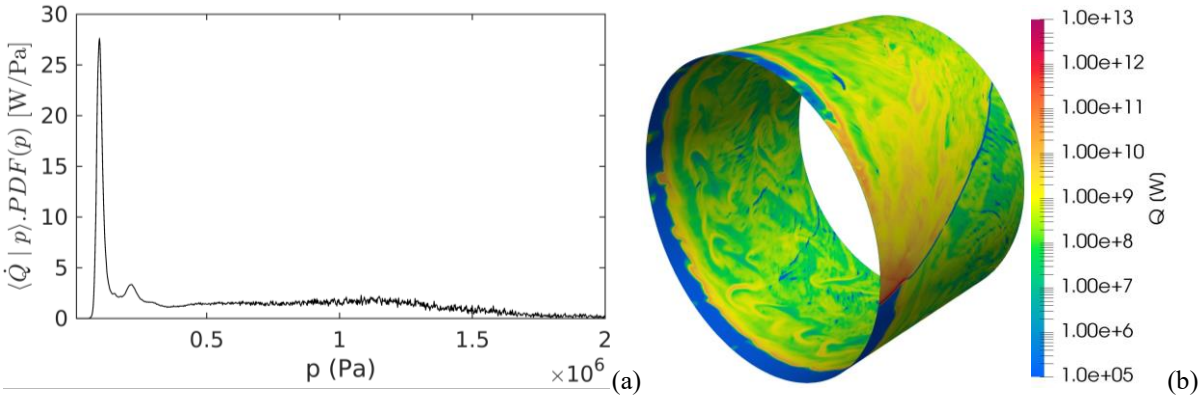

Fig 8. (a) Graph of heat release rate conditioned on pressure and scaled by probability density function, $\langle \dot{Q} \mid p \rangle \wp$ (b) instantaneous heat release rate, $\dot{Q}$, contour plot of a mid-channel (radial thickness) plane showing detonation and deflagration effects. Note that a log-scale is used in (b).

Progressing beyond direct statistical evaluation of purely conditional data, which might not reveal the complete picture, the LES data was scaled with the Probability Density Function (PDF), $\wp$, to factor in the probability of occurrence for each state. Shown in Fig. 8a is the plot of conditional heat release rate in pressure space, which has been scaled by the PDF, $\langle \dot{Q} \mid p \rangle \wp(p)$. The area under the graph gives the total heat release rates for a given range of pressure. The sharp peak around atmospheric pressure could be attributed to energy release from deflagration, which is also commonly known as isobaric combustion, whereas the flatter yet wide regions of heat release at elevated pressures is a derivative of pressure-gaining detonative combustion. It can be concluded that the contribution to $\dot{Q}$ from the two combustion modes are comparable, and a wide range of pressures occurs within the detonation regime.

In the instantaneous $\dot{Q}$ contour plot of a mid-channel plane shown in Fig. 8b, the extremely large range of heat release within an RDC is apparent. Moreover, although the highest levels of $\dot{Q}$ occur behind the detonation wave and oblique shock, extending over a sizeable region, large amounts of heat release take place nearly throughout the whole plane. This aligns with the peak $\langle \dot{\mathrm{Q}} \mid \mathrm{p} \rangle \wp(p)$ addressed in the previous paragraph, given the fact that the lower-energy-generating deflagration is very prevalent in the chamber. Upon further examination of Fig. 8b, parasitic combustion could also be identified at the interface between cold reactants (in blue) and hot gases from previous wave cycle axially downstream, as well as from some streams of fuel (green streaks) just after leaving the injectors. Commonly termed as parasitic combustion, such pre-detonation deflagrative burning would prematurely begin the combustion of reactants, causing the eventual detonation to be less efficient and potentially contributing to its unsteadiness. These factors might altogether have, at least partly, contributed to the nullification of any pressure-elevating effects of detonation such that overall pressure gain has yet to be observed in RDCs.

5. Conclusions

High-fidelity simulations were conducted on a H_2-air non-premixed RDC modelled after an AFRL design to yield a 3D perspective on the internal flow dynamics. The investigation was done with a fixed mass flow rate of 0.144 kg/s. The simulation attained a self-sustaining single detonation wave mode,

capturing signature wave structures. The LES model showed time-averaged chamber pressure, $\langle p_{ch} \rangle$, trends in line with experimental results, albeit predicting a higher wave frequency of 3.8 kHz.

Through analysis of the results, including contour plots and quantitative data, key wave characteristics have been identified. The detonation wave and the associated oblique shock brought about volumetric expansions, and regions of elevated temperature and pressure which temporarily suppressed fuel injection. The expansion occurred in both the azimuthal and radial directions, contributing to a forward curving main wave front and higher outer wall temperatures for the upstream axial half of the combustor.

Conditional statistics revealed that the extent of mixing has a significant influence on the combustion processes. Inconsistent and inhomogeneous reactant mixes led to varying detonation wave strength and structure, giving rise to the fluctuating effects the passing wave brings upon the RDC flow fields. Deflagrative combustion is also found to play an important role in the simulated case, occurring in large portions of the chamber and also having appreciable contributions in terms of $\dot{Q}$. When occurring downstream of the detonation wave, deflagration contributes to low-level exothermicity; the process has a parasitic impact when it takes place prior to the main wave sweep, reducing the resultant strength of the detonative combustion.

Acknowledgement

Computational time was partly provided by the Swedish National Infrastructure for Computing, partially funded by the Swedish Research Council through grant agreement no. 2018-05973, and partly provided by LUNARC.

References

1. Heiser, W.H. and D.T. Pratt, *Thermodynamic cycle analysis of pulse detonation engines.* Journal of propulsion and power, 2002. **18**(1): p. 68-76.
2. Anand, V. and E. Gutmark, *Rotating detonation combustors and their similarities to rocket instabilities.* Progress in Energy and Combustion Science, 2019. **73**: p. 182-234.
3. Holley, A., *Combined Cycle Power Generation Employing Pressure Gain Combustion*. 2017, United Technologies Corporation, East Hartford, CT (United States).
4. Zhao, M. and H. Zhang, *Large eddy simulation of non-reacting flow and mixing fields in a rotating detonation engine.* Fuel, 2020. **280**: p. 118534.
5. St. George, A.C., et al. *Fuel blending as a means to achieve initiation in a rotating detonation engine*. in *53rd AIAA aerospace sciences meeting*. 2015.
6. Bykovskii, F.A. and E.F. Vedernikov, *Continuous Detonation of a Subsonic Flow of a Propellant.* Combustion, Explosion, & Shock Waves, 2003. **39**(3).
7. Kindracki, J., P. Wolański, and Z. Gut, *Experimental research on the rotating detonation in gaseous fuels–oxygen mixtures.* Shock waves, 2011. **21**: p. 75-84.
8. Jin, S., et al., *Experimental and numerical research on rotating detonation combustor under non-premixed conditions.* International Journal of Hydrogen Energy, 2020. **45**(16): p. 10176-10188.
9. Nejaamtheen, M.N., J.-M. Kim, and J.-Y. Choi, *Review on the research progresses in rotating detonation engine.* Detonation Control for Propulsion: Pulse Detonation and Rotating Detonation Engines, 2018: p. 109-159.
10. Frolov, S., et al. *Demonstrator of continuous-detonation air-breathing ramjet: Wind tunnel data*. in *Doklady Physical Chemistry*. 2017. Springer.
11. Heister, S., D. Stechmann, and D. Lim, *Experimental Study of a High Pressure Rotating Detonation Wave Combustor for Rocket Applications.*

12. Liu, S.-J., et al., *Experimental and three-dimensional numerical investigations on H2/air continuous rotating detonation wave.* Proceedings of the Institution of Mechanical Engineers, Part G: Journal of Aerospace Engineering, 2013. **227**(2): p. 326-341.
13. Fujii, J., et al., *Numerical investigation on detonation velocity in rotating detonation engine chamber.* Proceedings of the Combustion Institute, 2017. **36**(2): p. 2665-2672.
14. He, X.-J., X.-Y. Liu, and J.-P. Wang, *Numerical study of the mechanisms of the longitudinal pulsed detonation in two-dimensional rotating detonation combustors.* Physics of Fluids, 2023. **35**(3): p. 036123.
15. Zhdan, S.A., F.A. Bykovskii, and E.F. Vedernikov, *Mathematical modeling of a rotating detonation wave in a hydrogen-oxygen mixture.* Combustion, explosion, and shock waves, 2007. **43**: p. 449-459.
16. Frolov, S., A. Dubrovskii, and V. Ivanov, *Three-dimensional numerical simulation of operation process in rotating detonation engine.* Progress in Propulsion Physics, 2013. **4**: p. 467-488.
17. Smirnov, N., et al., *Rotating detonation in a ramjet engine three-dimensional modeling.* Aerospace Science and Technology, 2018. **81**: p. 213-224.
18. Sun, Z., et al., *Three-dimensional simulation of a rotating detonation engine in ammonia/hydrogen mixtures and oxygen-enriched air.* International Journal of Hydrogen Energy, 2023. **48**(12): p. 4891-4905.
19. Dinh, T.X., M. Yoshida, and S. Ishikura, *Simulation of rotating detonation engine by OpenFOAM.* Sci. Tech Energetic Materials, 2019. **80**(2): p. 68-71.
20. Ye-Tao, S. and W. Jian-Ping, *Three dimensional simulation of rotating detonation engine without inner wall.* 23rd ICDERS, 2011: p. 24-29.
21. Yao, S., et al., *Numerical study of rotating detonation engine with an array of injection holes.* Shock Waves, 2017. **27**: p. 467-476.
22. Levin, V.A., I.S. Manuylovich, and V.V.e. Markov, *Rotating detonation wave in an annular gap.* Proceedings of the Steklov Institute of Mathematics, 2018. **300**: p. 126-136.
23. Lietz, C., et al. *Parametric investigation of rotating detonation rocket engines using large eddy simulations*. in *AIAA Propulsion and Energy 2019 Forum*. 2019.
24. Rankin, B.A., et al., *Chemiluminescence imaging of an optically accessible non-premixed rotating detonation engine.* Combustion and Flame, 2017. **176**: p. 12-22.
25. Codoni, J.R., et al. *Simultaneous mid-IR H2O/CO2 emission and OH chemiluminesence measurements within a RDE operating with and without backpressure*. in *2018 AIAA Aerospace sciences meeting*. 2018.
26. Fugger, C.A., et al., *The dynamics of a non-premixed rotating detonation engine from time-resolved temperature measurements.* Proceedings of the Combustion Institute, 2021. **38**(3): p. 3787-3795.
27. Rein, K.D., et al., *Measurements of gas temperatures at 100 kHz within the annulus of a rotating detonation engine.* Applied Physics B, 2017. **123**: p. 1-9.
28. Pal, P., et al., *Multidimensional numerical modeling of combustion dynamics in a non-premixed rotating detonation engine with adaptive mesh refinement.* Journal of Energy Resources Technology, 2021. **143**(11).
29. Yellapantula, S., et al. *A numerical study of H2-air rotating detonation combustor*. in *26th Int. Colloquium on the Dynamics of Explosion and Reactive Systems*. 2017.
30. Giacomazzi, E., F. Picchia, and N. Arcidiacono. *On the distribution of Lewis and Schmidt numbers in turbulent flames*. in *30th Italian Meeting on Combustion, Ischia, Italy*. 2007. Citeseer.

31. Menon, S. and C. Fureby, *Computational combustion.* Encyclopedia of Aerospace Engineering, 2010.
32. Gaillard, T., D. Davidenko, and F. Dupoirieux, *Numerical simulation of a rotating detonation with a realistic injector designed for separate supply of gaseous hydrogen and oxygen.* Acta Astronautica, 2017. **141**: p. 64-78.
33. Fureby, C. and F.F. Grinstein, *Large eddy simulation of high-Reynolds-number free and wall-bounded flows.* Journal of Computational Physics, 2002. **181**(1): p. 68-97.
34. Fureby, C., et al., *An experimental and computational study of a multi-swirl gas turbine combustor.* Proceedings of the Combustion Institute, 2007. **31**(2): p. 3107-3114.
35. Drikakis, D., et al., *ILES with limiting algorithms.* Implicit Large Eddy Simulation: Computing Turbulent Fluid Dynamics, Eds. Grinstein FF, Margolin L. & Rider B., Cambridge University Press, 2007. **94**.
36. Weller, H.G., et al., *A tensorial approach to computational continuum mechanics using object-oriented techniques.* Computers in physics, 1998. **12**(6): p. 620-631.
37. Fureby, C., *Challenges for large eddy simulation of engineering flows.* Whither Turbulence and Big Data in the 21st Century?, 2017: p. 375-400.
38. Kawai, S. and S.K. Lele, *Localized artificial diffusivity scheme for discontinuity capturing on curvilinear meshes.* Journal of Computational Physics, 2008. **227**(22): p. 9498-9526.
39. Adams, N.A. and K. Shariff, *A high-resolution hybrid compact-ENO scheme for shock-turbulence interaction problems.* Journal of Computational Physics, 1996. **127**(1): p. 27-51.
40. Kurganov, A. and E. Tadmor, *New high-resolution central schemes for nonlinear conservation laws and convection–diffusion equations.* Journal of computational physics, 2000. **160**(1): p. 241-282.
41. Strang, G., *On the construction and comparison of difference schemes.* SIAM journal on numerical analysis, 1968. **5**(3): p. 506-517.
42. Ordinary, H.E.W.G.S., *Differential Equations II.* Stiff and Differential-Algebraic Problems, 1991.
43. Fedina, E., et al., *Assessment of finite rate chemistry large eddy simulation combustion models.* Flow, Turbulence and Combustion, 2017. **99**: p. 385-409.
44. Nilsson, T., S. Zhong, and C. Fureby, *LES of H2-air jet combustion in high enthalpy supersonic crossflow.* Physics of Fluids, 2021. **33**(3): p. 035133.
45. Marinov, N., C. Westbrook, and W. Pitz, *Detailed and global chemical kinetics model for.* Transp. Phenom. Combust, 1996. **1**: p. 118.
46. Eklund, D. and S. Stouffer. *A numerical and experimental study of a supersonic combustor employing sweep ramp fuel injectors*. in *30th Joint Propulsion Conference and Exhibit*. 1994.
47. Baurle, R. and S. Girimaji, *Assumed PDF turbulence-chemistry closure with temperature-composition correlations.* Combustion and Flame, 2003. **134**(1-2): p. 131-148.
48. Davidenko, D., et al., *Numerical simulation of hydrogen supersonic combustion and validation of computational approach*, in *12th AIAA international space planes and hypersonic systems and technologies*. 2003. p. 7033.
49. Jachimowski, C.J., *An analytical study of the hydrogen-air reaction mechanism with application to scramjet combustion*. 1988.

50. Alekseev, V.A., M. Christensen, and A.A. Konnov, *The effect of temperature on the adiabatic burning velocities of diluted hydrogen flames: A kinetic study using an updated mechanism.* Combustion and flame, 2015. **162**(5): p. 1884-1898.
51. Wang, H., et al., *USC Mech Version II. High-temperature combustion reaction model of H2/CO/C1-C4 compounds.* URL: http://ignis. usc. edu/USC_Mech_II. htm, 2007.
52. Zettervall, N. and C. Fureby. *A computational study of ramjet, scramjet and dual-mode ramjet combustion in combustor with a cavity flameholder*. in *2018 AIAA aerospace sciences meeting*. 2018.
53. Larsson, A., et al., *Skeletal methane–air reaction mechanism for large eddy simulation of turbulent microwave-assisted combustion.* Energy & Fuels, 2017. **31**(2): p. 1904-1926.
54. Slack, M. and A. Grillo, *Investigation of hydrogen-air ignition sensitized by nitric oxide and by nitrogen dioxide. Final report*. 1977, Grumman Aerospace Corp., Bethpage, NY (USA).
55. Samuelsen, S., et al., *Correlation of ignition delay with natural gas and IGCC type fuels.* Univ. of California, Irvine, 2006.
56. Snyder, A., et al., *Shock tube studies of fuel-air ignition characteristics*. 1965, MONSANTO RESEARCH CORP DAYTON OH.
57. Kwon, O. and G. Faeth, *Flame/stretch interactions of premixed hydrogen-fueled flames: measurements and predictions.* Combustion and Flame, 2001. **124**(4): p. 590-610.
58. Dowdy, D.R., et al. *The use of expanding spherical flames to determine burning velocities and stretch effects in hydrogen/air mixtures*. in *Symposium (International) on Combustion*. 1991. Elsevier.
59. Juniper, M., N. Darabiha, and S. Candel, *The extinction limits of a hydrogen counterflow diffusion flame above liquid oxygen.* Combustion and flame, 2003. **135**(1-2): p. 87-96.
60. Schwer, D. and K. Kailasanath. *Numerical investigation of rotating detonation engines*. in *46th AIAA/ASME/SAE/ASEE joint propulsion conference & exhibit*. 2010.
61. Raman, V., S. Prakash, and M. Gamba, *Nonidealities in Rotating Detonation Engines.* Annual Review of Fluid Mechanics, 2023. **55**.
62. Prakash, S., et al., *Numerical simulation of a methane-oxygen rotating detonation rocket engine.* Proceedings of the Combustion Institute, 2021. **38**(3): p. 3777-3786.
63. Sato, T., et al., *Mixing and detonation structure in a rotating detonation engine with an axial air inlet.* Proceedings of the Combustion Institute, 2021. **38**(3): p. 3769-3776.
64. Bilger, R., *Conditional moment closure for turbulent reacting flow.* Physics of Fluids A: Fluid Dynamics, 1993. **5**(2): p. 436-444.

